Letter

Interpretable and Efficient Interferometric Contrast in Scanning Transmission Electron Microscopy with a Diffraction-Grating Beam Splitter

Tyler R. Harvey,[1,2] Fehmi S. Yasin,[1] Jordan J. Chess,[1] Jordan S. Pierce,[1] Roberto M. S. dos Reis,[3] Vasfi Burak Özdöl,[3] Peter Ercius,[3] Jim Ciston,[3] Wenchun Feng,[4,5] Nicholas A. Kotov,[4,6] Benjamin J. McMorran,[1,*] and Colin Ophus[3]

[1] *Department of Physics, University of Oregon, Eugene, Oregon 97403, USA*
[2] *Georg-August-Universität Göttingen, D-37077 Göttingen, Germany*
[3] *National Center for Electron Microscopy, Molecular Foundry, Lawrence Berkeley National Laboratory, Berkeley, California 94720, USA*
[4] *Department of Chemical Engineering, University of Michigan, Ann Arbor, Michigan 48109, USA*
[5] *US Food and Drug Administration, Silver Spring, Maryland 20993, USA*
[6] *Department of Materials Science and Engineering, University of Michigan, Ann Arbor, Michigan 48109, USA*

(Received 6 August 2018; revised manuscript received 5 November 2018; published 26 December 2018)

Efficient imaging of biomolecules, two-dimensional materials, and electromagnetic fields depends on retrieval of the phase of transmitted electrons. We demonstrate a method to measure phase in a scanning transmission electron microscope (STEM) using a nanofabricated diffraction grating to produce multiple probe beams. The measured phase is more interpretable than phase-contrast scanning transmission electron microscopy techniques without an off-axis reference wave, and the resolution could surpass that of off-axis electron holography. We apply this technique, called STEM holography, to image nanoparticles, carbon substrates, and electric fields. The contrast observed in experiments agrees well with contrast predicted in simulations.

DOI: 10.1103/PhysRevApplied.10.061001

I. INTRODUCTION

Material structure and physical processes can be directly imaged at atomic length scales in electron microscopes. Whereas bulk measurements must be interpreted to infer the microscopic structure or processes, in the transmission electron microscope (TEM) one can directly measure the atomic number and positions of atoms and atomic columns, local shifts in atomic transition energies, and electronic and magnetic properties with high precision [1–5]. Scanning transmission electron microscopy (STEM) with an annular dark-field detector (ADF) has long offered highly interpretable contrast at atomic resolution [3,6].

However, ADF-STEM requires a high dose for a good signal-to-noise ratio even on highly scattering high-atomic-number materials; resolution is limited on dose-sensitive, weakly scattering low-atomic-number materials by noise or structure-altering damage [7]. Efficient imaging depends on measurement of phase shifts acquired by an electron passing through a specimen. The most common phase-contrast imaging method employs a small defocus for contrast in high-resolution transmission electron microscopy (HRTEM) [8]. However, this contrast can be difficult to interpret without a focal series [9]. Several STEM techniques offer similarly efficient and more interpretable contrast.

The development of quadrant detectors and high-frame-rate direct detectors has enabled "4D STEM" techniques that utilize one diffraction pattern per probe position. Differential phase contrast (DPC), center of mass (CoM), ptychography, and matched illumination and detector interferometry (MIDI) offer dose-efficient alternatives for interpretable phase contrast in STEM [10–12,12–18]. However, these STEM techniques and HRTEM measure only local phase variations, making quantitative thickness measurement difficult and long-range electric- and magnetic-field measurement inefficient.

Off-axis electron holography offers more interpretable phase measurement with respect to a vacuum reference wave. This allows, for example, imaging of magnetic bits in recording media [19] and insight into the charge distribution and asymmetry of nanoparticles [20]. However, as interference fringes are in real space, resolution is limited by the fringe spacing [21]. We demonstrate a method to measure specimen-induced electron phase shifts from the interference of multiple STEM probes produced

*mcmorran@uoregon.edu

with an electron diffraction grating. Because the throughput of pixelated detectors was insufficient, early forms of STEM holography with a biprism beam splitter [22] either employed a grating to map fringe shifts into one intensity per probe position [23,24] or used no scanning [25–27]. We can now directly image interference fringes at each probe position with a pixelated detector.

Diffraction gratings have several advantages over biprisms as beam splitters for STEM holography. The coherence width necessary for optimal fringe visibility is much lower for an amplitude-dividing beam splitter than a wave-front-dividing beam splitter [28–30]. Biprisms produce two opposing half-circular probes in reciprocal space, whereas grating-produced probes can have identical phase and amplitude distributions. Phase structuring can extend STEM holography to map out-of-plane magnetic fields [31–35] (see Section III of the Supplemental Material [36]) or correct aberrations [37–39]. We have previously demonstrated a three-beam STEM interferometer and proposed a phase reconstruction method for probe sizes much smaller than specimen phase variations [40]. Here, we develop a general approach to reconstruct phase from two or more beams with a tunable phase structure. We then treat the two-beam case in detail and experimentally demonstrate the method.

II. MODEL AND RECONSTRUCTION

A. General case

We use a prespecimen probe wave function

$$\psi_i(\mathbf{x}) = a(\mathbf{x}-\mathbf{x}_p), \tag{1}$$

where $\mathbf{x}_p$ is the offset position of our probe. For thin specimens and ignoring inelastic scattering, we may use a specimen transmission function $t(\mathbf{x})$ to describe the interaction:

$$\psi_f(\mathbf{x}) = a(\mathbf{x}-\mathbf{x}_p)t(\mathbf{x}). \tag{2}$$

The measured reciprocal-space interference pattern $I_p(\mathbf{k}) = \left|\psi_f(\mathbf{k})\right|_p^2$ at probe position $\mathbf{x}_p$ is

$$I_p(\mathbf{k}) = \left[A_p^*(\mathbf{k}) \otimes T^*(\mathbf{k})\right]\left[A_p(\mathbf{k}) \otimes T(\mathbf{k})\right], \tag{3}$$

where $A_p(\mathbf{k})$ is the Fourier transform of $a(\mathbf{x}-\mathbf{x}_p)$ and $T(\mathbf{k})$ is the Fourier transform of $t(\mathbf{x})$.

The sharply peaked, evenly spaced probes produced by a diffraction grating have a real-space wave function

$$a(\mathbf{x}-\mathbf{x}_p) = \sum_m c_m a_m(\mathbf{x}-m\mathbf{x}_0-\mathbf{x}_p), \tag{4}$$

where $a_m(\mathbf{x})$ is peaked at $\mathbf{x}=\mathbf{0}$. In reciprocal space,

$$A_p(\mathbf{k}) = \sum_m c_m e^{-i\mathbf{k}\cdot(m\mathbf{x}_0+\mathbf{x}_p)} A_m(\mathbf{k}). \tag{5}$$

If we plug this into (3) and move the plane-wave terms through the convolution [41], we find

$$I_p(\mathbf{k}) = \sum_{m,n} c_m^* c_n \left[A_m^*(\mathbf{k}) \otimes \left(T^*(\mathbf{k}) e^{-i\mathbf{k}\cdot(m\mathbf{x}_0+\mathbf{x}_p)}\right)\right] \cdot \left[A_n(\mathbf{k}) \otimes \left(T(\mathbf{k}) e^{i\mathbf{k}\cdot(n\mathbf{x}_0+\mathbf{x}_p)}\right)\right] e^{-i(n-m)\mathbf{k}\cdot\mathbf{x}_0}. \tag{6}$$

The specimen transmission function $t(\mathbf{x})$ is encoded in the set of plane waves $e^{-i(n-m)\mathbf{k}\cdot\mathbf{x}_0}$.

Plane waves in (6) become spatially separated spots after an inverse Fourier transform:

$$\mathcal{I}(\mathbf{x}_p,\mathbf{x}) = \frac{1}{2\pi}\int d\mathbf{k}\, e^{i\mathbf{k}\cdot\mathbf{x}} I_p(\mathbf{k}) = \sum_\ell \mathcal{I}_\ell(\mathbf{x}_p,\mathbf{x}), \tag{7}$$

where $\ell = n-m$ and each $\mathcal{I}_\ell$ term contains a sum over m. $\mathcal{I}_0$ corresponds to $n=m$ terms that contain information only on the amplitude of the specimen transmission function [42]. $\mathcal{I}_{-1}$ contains the same information as $\mathcal{I}_1$. Each $\mathcal{I}_\ell(\mathbf{x}_p,\mathbf{x})$ is sharply peaked at $\mathbf{x}=\ell\mathbf{x}_0$. Let us focus on a few plane waves to gain a better insight into the information encoded there.

B. Two beams, vacuum reference

Off-axis electron holography has only two interfering plane waves and, correspondingly, a straightforward fringe pattern. We can introduce a condenser aperture or a selected-area aperture, as we use here, to select two beams. We will consider the case where all but the $m=0$ and $m=+1$ beams are blocked and $m=0$ passes through vacuum, i.e., $t(\mathbf{x})=1$ near $\mathbf{x}=0$ over a region larger than the scanned area. We assume that the aperture function $A_m = A_0$ is the same for both diffraction orders and is a uniform disk:

$$A_0(\mathbf{k}) = \begin{cases} \dfrac{1}{\sqrt{\pi K^2}}, & |\mathbf{k}| \le K, \\ 0, & |\mathbf{k}| > K, \end{cases} \tag{8}$$

where K is the aperture edge.

Now, only $\mathcal{I}_{-1}$, $\mathcal{I}_0$, and $\mathcal{I}_1$ are nonzero and contain only a single term from the sum on m. $\mathcal{I}_1$ contains the important information:

$$\mathcal{I}_1(\mathbf{x}_p,\mathbf{x}) = c_0^* c_1 a_0(\mathbf{x}) \otimes \left[a_0(\mathbf{x}) t(\mathbf{x}+\mathbf{x}_0+\mathbf{x}_p)\right]. \tag{9}$$

We want an interpretable function of just $\mathbf{x}_p$ but we have two position variables.

The simplest way to trace one out is to integrate over $\mathbf{x}$ in a limited window around $\mathcal{I}_1$, with $a_0(\mathbf{x})$ as a kernel. We use a window width $0.08|\mathbf{x}_0|$. This is mathematically equivalent to numerically applying an aperture around $\mathcal{I}_1$, taking a Fourier transform, and integrating over the diffraction

disk, analogous to the reconstruction method in electron holography:

$$t_M(\mathbf{x}_p + \mathbf{x}_0) = -\frac{\sqrt{\pi K^2}}{c_0^* c_1} \int d\mathbf{x}\, a_0(\mathbf{x}) \mathcal{I}_1(\mathbf{x}_p, \mathbf{x}) = h(\mathbf{x}_p) \otimes t(\mathbf{x}_p + \mathbf{x}_0). \quad (10)$$

The measured transmission function, t_M, is exactly the specimen transmission function convolved with a point-spread function (PSF) $h(\mathbf{x}_p) = |a_0(\mathbf{x}_p)|^2$. A nontrivial aperture function only changes $h(\mathbf{x}_p)$ in (10), as we show in Sections II and III of the Supplemental Material [36]. Even with aberrations, this PSF is *always real*; the phase and amplitude signals never mix. In electron holography, however, finite aberrations produce a complex PSF that limits quantitative interpretation of the phase and amplitude at high resolution [43]. The integrated phase over a region larger than the PSF is always conserved in STEM holography. We can gain more insight into the effect of this PSF on our image by looking at its reciprocal space equivalent, the contrast transfer function (CTF) [44].

The CTF measures the efficiency with which an imaging method reconstructs the spatial frequencies in an image. The nearly unity efficiency as the spatial frequency approaches zero, shown in Fig. 3, is a unique feature of STEM holography. Unlike existing phase-contrast STEM techniques, where the value of the reconstructed phase of any one pixel is meaningful only with respect to its neighbors in some finite-sized region, in STEM holography, the phase recorded in one pixel offers a meaningful comparison to an electron passed through vacuum. STEM holography can therefore quantitatively measure thickness or electric and magnetic fields. Indeed, with a convergence angle larger than the deflection angle due to a field, STEM holography is more precise than CoM STEM.

III. EXPERIMENT

We test our implementation of STEM holography on three types of specimens: a lacey carbon substrate, gold nanoparticles on lacey and ultrathin carbon, and semiconducting CdTe/CdS nanoparticles synthesized according to procedures described previously [45,46].

To produce multiple diffracted beams, we place a 50 μm-diameter diffraction grating with a 150 nm pitch [see Fig. 2(a)] in the third condenser-aperture strip of the TEAM I microscope at the Lawrence Berkeley National Laboratory. The second condenser aperture is used to block transmission outside the grating. The selected-area aperture is used to pass only two beams. As the profile of peaks in the grating is slightly asymmetric, the amplitudes (normalized to selected-area transmission) of the zeroth- and first-order beams are $c_0 = 0.79$ and $c_1 = 0.61$, respectively [see Fig. 2(d)]. We measure an interference fringe visibility $V = 70.7\%$. As the maximum possible for our measured beam amplitudes c_0 and c_1 is $V = 96.7\%$, our measured value is likely lower due to inelastic scattering in the grating, aberrations in the projector lens system, and an imperfect detector modulation-transfer function (MTF).

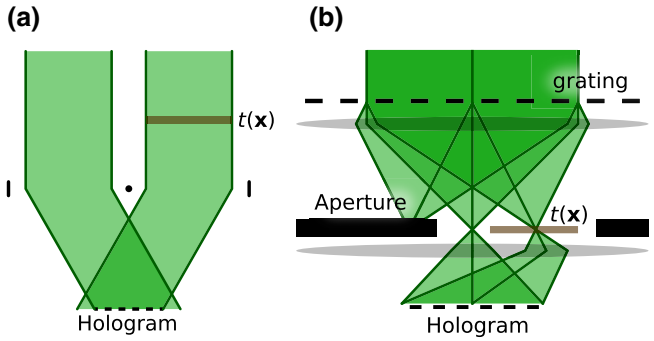

FIG. 1. (a) A schematic of off-axis electron holography with a biprism. One plane wave is passed through the specimen (brown) and an electrostatic biprism (black dot) interferes this wave with a second plane wave passed through vacuum. (b) A schematic of STEM holography. A diffraction grating in the condenser system produces multiple beams at the specimen (brown). An aperture (black) admits one beam that interacted with the specimen and one passed through vacuum. The projector system combines these beams into a hologram.

We use a 300 keV electron energy and a 4 mrad convergence semiangle, and we record data using the Gatan K2 IS detector at 400 fps with a $L = 1.45$ m camera length.

The phase measured by STEM holography and the ADF-STEM signal agree very well on lacey carbon, as shown in Fig. 4(g). Since lacey carbon has no diffraction contrast and is conductive, both techniques produce mass-thickness contrast.

However, on and near a semiconducting nanoparticle, charging of the particle strongly affects the phase and does not affect the ADF, as shown in Fig. 4(h). The organic stabilizers used in the synthesis of the nanoparticles may persist on the surface and contribute to charging [20]. There are clusters on the surface of the particles that may be electrically insulated. The clusters can be seen most clearly in the ADF [Fig. 4(f)]. As the clusters do not stand out in the phase image [Fig. 4(e)], it is likely that the average atomic number of the clusters is close to that of the particles but that the crystalline order produces diffraction contrast.

Imaging with STEM holography also works with the reference beam on a uniform substrate if no vacuum region is accessible. In Fig. 5, we pass the reference beam through ultrathin carbon and scan the imaging beam over a gold nanoparticle on ultrathin carbon. Increased noise is likely with high doses on a reference area of a uniform substrate, as STEM holography is highly sensitive to deposited contamination. The spot that is barely distinguishable from noise in the upper left of the ADF image [Fig. 5(d)] is

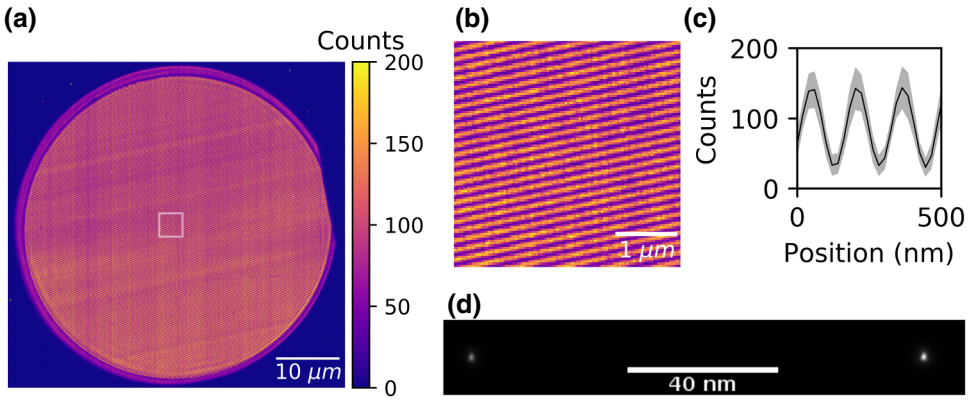

FIG. 2. (a) Measured interference fringes formed by two beams in vacuum. (b) An enlargement of the region in (a) highlighted by a white rectangle (same color bar). (c) A line profile (black) with a 95% confidence interval (gray) of interference fringes in the center of (a). (d) A micrograph of the beams used for the experiment. The beam separation is $|\mathbf{x}_0| = 120$ nm.

quite clear on the phase image [Fig. 5(b)]. So, if the reference beam deposits contamination, the imaged phase will include contributions from the uncharacterized phase of the reference area, which is effectively noise.

Although the phase measured by STEM holography produces more efficient contrast, the amplitude also offers valuable information. The amplitude image is similar to a bright-field image, but with linear rather than quadratic sensitivity to amplitude changes in the bright-field disk. With our low convergence angle, diffraction produces only amplitude contrast. Strong linear phases from particle edges cause a shift in diffraction and therefore a reduced overlap of the two disks, so the amplitude image has good edge contrast. A combined phase-amplitude image is sometimes more interpretable than either alone, as seen in Fig. 5(c).

Simulations of a STEM-holography experiment with beam separation $x_0 = 15$ nm and a 4-mrad convergence semiangle, on gold particles embedded in an amorphous carbon wedge [47], support our experimental observations, as shown in Fig. 6. The PRISM algorithm [48] implemented in the Prismatic code [49] is used to produce each probe simulation, these then being combined coherently in reciprocal space to form STEM-holography diffraction patterns. The phase [Fig. 6(b)] more clearly matches the projected potential [Fig. 6(d)] than the ADF signal [Fig. 6(c)], as the contrast is much stronger on the carbon wedge. For a more detailed comparison of the phase and projected potential, see Section VIII of the Supplemental Material [36]. As we use an ADF detector inner semiangle of 8 mrad, we see diffraction contrast in both the ADF and amplitude signals.

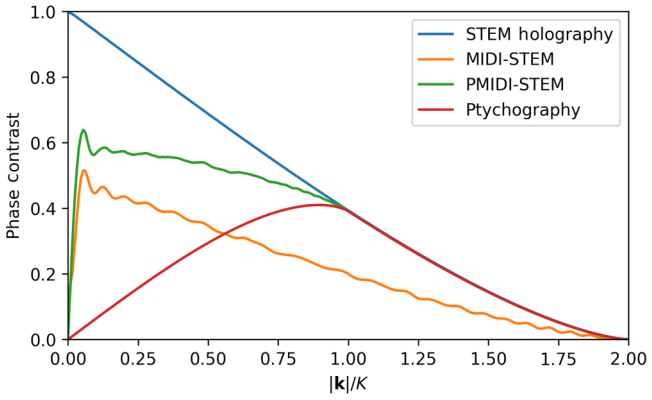

FIG. 3. A comparison of the calculated phase-contrast transfer functions for several phase-contrast STEM techniques. Unlike MIDI-STEM [18], PMIDI-STEM [16], and ptychography [17], STEM holography produces efficient contrast as the spatial frequency approaches zero (see (10)).

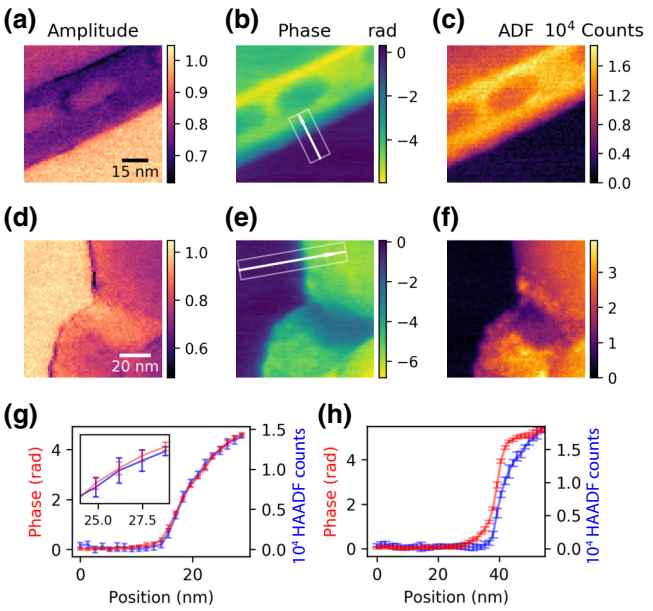

FIG. 4. A comparison of micrographs recorded by STEM holography and ADF-STEM on lacey carbon and semiconducting nanoparticles. (a),(d) The amplitude measured by STEM holography. (b),(e) The phase measured by STEM holography; the line profiles in (g) and (h) are taken along the white arrow and averaged over the width of the box. (c),(f) The simultaneously acquired ADF. (g) A comparison of the phase (red) with the ADF (blue) on a lacey carbon edge. Inset: an enlargement to show the noise levels. (h) The same as (g) on the edge of a semiconducting nanoparticle.

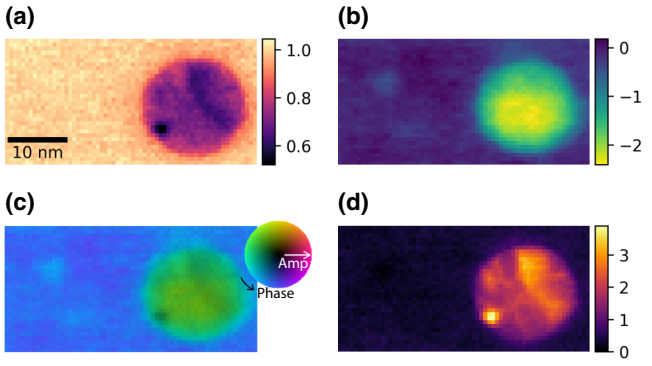

FIG. 5. An Au nanoparticle with a reference beam on a uniform ultrathin carbon substrate. (a) The amplitude from STEM holography. (b) The phase from STEM holography. (c) The phase (color) and amplitude (brightness) shown together offer more information than either alone. The color wheel maximum brightness corresponds to the maximum amplitude in the image and black corresponds to zero amplitude. (d) The simultaneously acquired ADF signal.

We see from experimental tests and comparison with simulation that STEM holography offers efficient contrast on low- and high-atomic-number materials as well as on electric fields. In particular, like ADF-STEM, but unlike other phase-contrast STEM techniques, the CTF does not go to zero at zero spatial frequency (Fig. 3), so that efficient quantitative thickness and electromagnetic-field measurement are possible.

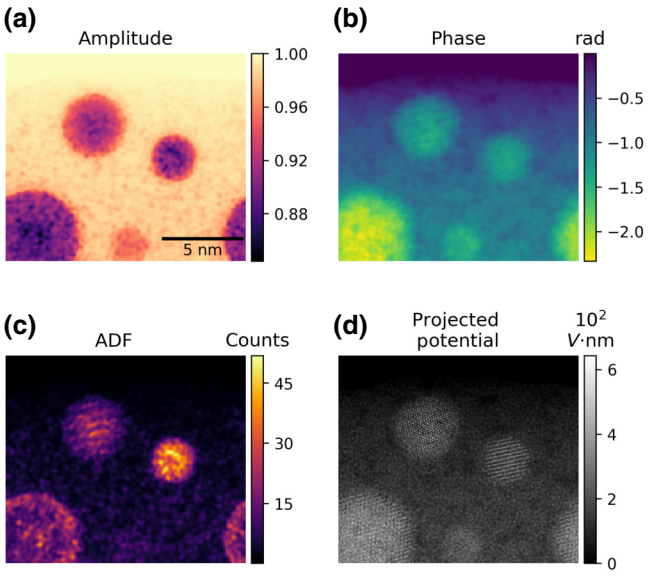

FIG. 6. The simulated STEM-holography dataset with Au nanoparticles on a carbon wedge and a reference beam in vacuum. (a) The amplitude. (b) The phase. (c) The ADF from the same dataset. (d) The projected potential used to generate the dataset.

IV. CONCLUSION

We demonstrate a straightforward method to measure the transmission function of a specimen with STEM holography. Unlike existing phase-contrast STEM techniques, STEM holography measures phase with respect to a vacuum reference. A single pixel in STEM holography therefore has an absolute meaning, just as in ADF-STEM. STEM holography also produces a lower-noise image than ADF [see Fig. 4(g)], with much better contrast on weak-phase objects and sensitivity to electric and magnetic fields.

STEM holography also has the potential to achieve higher resolution than off-axis electron holography. Unlike electron holography, the fringe spacing does not affect resolution in STEM holography, since the fringes are in diffraction space. The real-space resolution is limited only by aberrations, coherence, and the convergence angle of the probe. We show in related work that atomic-resolution phase measurement is possible with a higher convergence angle and aberration correction [50].

An iterative reconstruction could, in the future, provide more information. Higher resolution may be possible [51] by iteratively updating the transmission function based on $\mathcal{I}_1(\mathbf{x}_p, \mathbf{x})$ rather than simply integrating out $\mathbf{x}$. An iterative algorithm can also more easily treat scans where all beams begin in vacuum and end on a specimen, using information from the first beam's interaction at position $\mathbf{x}_p$ to correct for the next beam's interaction at $\mathbf{x}_p$ and produce a flat phase reference for the first beam at position $\mathbf{x}_p + \mathbf{x}_0$. Both methods, while more computationally intensive, could significantly improve the utility of STEM holography in understanding the fine structural details of cells, organic semiconductor interfaces, and nanostructures.

This simple modification to the electron-microscope column—replacement of one condenser aperture with a diffraction grating—and straightforward reconstruction has the potential for versatile and efficient imaging. Like off-axis holography, STEM holography is sensitive to electric and magnetic fields and can image with a resolution comparable to that of ADF-STEM.

V. ACKNOWLEDGMENTS

We appreciate useful discussions with Hao Yang. T.R.H. performed work at the Molecular Foundry with support from the U.S. Department of Energy, Office of Science, Office of Workforce Development for Teachers and Scientists, Office of Science Graduate Student Research (SCGSR) program. The SCGSR program is administered by the Oak Ridge Institute for Science and Education for the DOE under contract number DESC0014664. Work at the Molecular Foundry was also supported by the Office of Science, Office of Basic Energy Sciences, of the U.S. Department of Energy under Contract No. DE-AC02-05CH11231. F.S.Y. acknowledges support

from the National Science Foundation Graduate Research Fellowship Program under Grant No. 1309047. T.R.H., F.S.Y., J.J.C., J.S.P., and B.J.M. acknowledge support from the U.S. Department of Energy, Office of Science, Basic Energy Sciences, under Award DE-SC0010466. R.M.S.dR., J.C., and C.O. acknowledge support from the U.S. Department of Energy Early Career Research Program. W.F. and N.A.K. acknowledge funding from the National Science Foundation under Grant No. 1463474. We thank the NVIDIA Corporation for donation of GPU resources.

[1] K. Suenaga, M. Tencé, C. Mory, C. Colliex, H. Kato, T. Okazaki, H. Shinohara, K. Hirahara, S. Bandow, and S. Iijima, Element-selective single atom imaging, Science **290**, 2280 (2000).

[2] D. A. Muller, L. F. Kourkoutis, M. Murfitt, J. H. Song, H. Y. Hwang, J. Silcox, N. Dellby, and O. L. Krivanek, Atomic-scale chemical imaging of composition and bonding by aberration-corrected microscopy, Science **319**, 1073 (2008).

[3] O. L. Krivanek, M. F. Chisholm, V. Nicolosi, T. J. Pennycook, G. J. Corbin, N. Dellby, M. F. Murfitt, C. S. Own, Z. S. Szilagyi, M. P. Oxley, S. T. Pantelides, and S. J. Pennycook, Atom-by-atom structural and chemical analysis by annular dark-field electron microscopy, Nature **464**, 571 (2010).

[4] T. C. Lovejoy, Q. M. Ramasse, M. Falke, A. Kaeppel, R. Terborg, R. Zan, N. Dellby, and O. L. Krivanek, Single atom identification by energy dispersive x-ray spectroscopy, Appl. Phys. Lett. **100**, 154101 (2012).

[5] Y. Yang, C.-C. Chen, M. C. Scott, C. Ophus, R. Xu, A. Pryor, L. Wu, F. Sun, W. Theis, J. Zhou, M. Eisenbach, P. R. C. Kent, R. F. Sabirianov, H. Zeng, P. Ercius, and J. Miao, Deciphering chemical order/disorder and material properties at the single-atom level, Nature **542**, 75 (2017).

[6] S. J. Pennycook and D. E. Jesson, High-resolution incoherent imaging of crystals, Phys. Rev. Lett. **64**, 938 (1990).

[7] R. F. Egerton, Control of radiation damage in the TEM, Ultramicroscopy **127**, 100 (2013).

[8] R. M. Glaeser, Invited review article: methods for imaging weak-phase objects in electron microscopy, Rev. Sci. Instrum. **84**, 111101 (2013).

[9] W. Wan, S. Hovmöller, and X. Zou, Structure projection reconstruction from through-focus series of highresolution transmission electron microscopy images, Ultramicroscopy **115**, 50 (2012).

[10] W. Hoppe, Beugung im inhomogenen Primätrahlwellenfeld. I. Prinzip einer Phasenmessung von Elektronenbeungungsinterferenzen, Acta Crystallogr. Sec. A: Crystal Phys. Diffr. Theor. Gen. Crystallogr. **25**, 495 (1969).

[11] N. Dekkers and H. Lang, Differential phase-contrast in a Stem, Optik **41**, 452 (1974).

[12] H. H. Rose, Phase contrast in scanning transmission electron microscopy, Optik **39**, 416 (1974).

[13] J. Chapman, P. Batson, E. Waddell, and R. Ferrier, Direct determination of magnetic domain-wall profiles by differential phase-contrast electron-microscopy, Ultramicroscopy **3**, 203 (1978).

[14] E. Waddell and J. Chapman, Linear imaging of strong phase objects using asymmetrical detectors in stem, Optik **54**, 83 (1979).

[15] J. M. Rodenburg, in *Advances in Imaging and Electron Physics*, edited by Hawkes (Elsevier, London, UK, 2008), Vol. 150, p. 87.

[16] H. Yang, P. Ercius, P. D. Nellist, and C. Ophus, Enhanced phase contrast transfer using ptychography combined with a pre-specimen phase plate in a scanning transmission electron microscope, Ultramicroscopy **171**, 117 (2016).

[17] H. Yang, R. N. Rutte, L. Jones, M. Simson, R. Sagawa, H. Ryll, M. Huth, T. J. Pennycook, M. L. H. Green, H. Soltau, Y. Kondo, B. G. Davis, and P. D. Nellist, Simultaneous atomic-resolution electron ptychography and Z-contrast imaging of light and heavy elements in complex nanostructures, Nat. Commun. **7**, 12532 (2016).

[18] C. Ophus, J. Ciston, J. Pierce, T. R. Harvey, J. Chess, B. J. McMorran, C. Czarnik, H. H. Rose, and P. Ercius, Efficient linear phase contrast in scanning transmission electron microscopy with matched illumination and detector interferometry, Nat. Commun. **7**, 10719 (2016).

[19] N. Osakabe, K. Yoshida, Y. Horiuchi, T. Matsuda, H. Tanabe, T. Okuwaki, J. Endo, H. Fujiwara, and A. Tonomura, Observation of recorded magnetization pattern by electron holography, Appl. Phys. Lett. **42**, 746 (1983).

[20] J.-Y. Kim, M.-G. Han, M.-B. Lien, S. Magonov, Y. Zhu, H. George, T. B. Norris, and N. A. Kotov, Dipole-like electrostatic asymmetry of gold nanorods, Sci. Adv. **4**, e1700682 (2018).

[21] H. Lichte, in *Advances in Optical and Electron Microscopy*, edited by T. Mulvey and C. J. R. Sheppard (Elsevier, London, UK, 1991), Vol. 12, p. 25.

[22] J. Cowley, Ultra-high resolution with off-axis STEM holography, Ultramicroscopy **96**, 163 (2003).

[23] T. Leuthner, H. Lichte, and K.-H. Herrmann, STEM-holography using the electron biprism, Phys. Status Solidi (A) **116**, 113 (1989).

[24] Y. Takahashi, Y. Yajima, M. Ichikawa, and K. Kuroda, Observation of magnetic induction distribution by scanning interference electron microscopy, Jpn. J. Appl. Phys. **33**, L1352 (1994).

[25] J. M. Cowley, High resolution side-band holography with a STEM instrument, Ultramicroscopy **34**, 293 (1990).

[26] M. Mankos, M. R. Scheinfein, and J. M. Cowley, Absolute magnetometry at nanometer transverse spatial resolution: Holography of thin cobalt films in a scanning transmission electron microscope, J. Appl. Phys. **75**, 7418 (1994).

[27] M. Mankos, A. A. Higgs, M. R. Scheinfein, and J. M. Cowley, Far-out-of-focus electron holography in a dedicated FEG STEM, Ultramicroscopy **58**, 87 (1995).

[28] L. Marton, Electron interferometer, Phys. Rev. **85**, 1057 (1952).

[29] L. Marton, J. A. Simpson, and J. A. Suddeth, Electron beam interferometer, Phys. Rev. **90**, 490 (1953).

[30] G. Matteucci, G. F. Missiroli, and G. Pozzi, Amplitude division electron interferometry, Ultramicroscopy **6**, 109 (1981).
[31] J. Verbeeck, H. Tian, and P. Schattschneider, Production and application of electron vortex beams, Nature **467**, 301 (2010).
[32] B. J. McMorran, A. Agrawal, I. M. Anderson, A. A. Herzing, H. J. Lezec, J. J. McClelland, and J. Unguris, Electron vortex beams with high quanta of orbital angular momentum, Science **331**, 192 (2011).
[33] V. Grillo, G. C. Gazzadi, E. Karimi, E. Mafakheri, R. W. Boyd, and S. Frabboni, Highly efficient electron vortex beams generated by nanofabricated phase holograms, Appl. Phys. Lett. **104**, 043109 (2014).
[34] T. R. Harvey, J. S. Pierce, A. K. Agrawal, P. Ercius, M. Linck, and B. J. McMorran, Efficient diffractive phase optics for electrons, New J. Phys. **16**, 093039 (2014).
[35] V. Grillo, T. R. Harvey, F. Venturi, J. S. Pierce, R. Balboni, F. Bouchard, G. C. Gazzadi, S. Frabboni, A. H. Tavabi, Z.-A. Li, R. E. Dunin-Borkowski, R. W. Boyd, B. J. McMorran, and E. Karimi, Observation of nanoscale magnetic fields using twisted electron beams, Nat. Commun. **8**, 689 (2017).
[36] See the Supplemental Material at http://link.aps.org/supplemental/10.1103/PhysRevApplied.10.061001 for a video illustrating STEM holography, notes on aberrations, phase-structured probes, Cowley's proposed methods, scan artifact correction, and the limits of the thin-specimen approximation.
[37] M. Linck, P. A. Ercius, J. S. Pierce, and B. J. McMorran, Aberration corrected STEM by means of diffraction gratings, Ultramicroscopy **182**, 36 (2017).
[38] V. Grillo, A. H. Tavabi, E. Yucelen, P.-H. Lu, F. Venturi, H. Larocque, L. Jin, A. Savenko, G. C. Gazzadi, R. Balboni, S. Frabboni, P. Tiemeijer, R. E. Dunin-Borkowski, and E. Karimi, Towards a holographic approach to spherical aberration correction in scanning transmission electron microscopy, Opt. Express **25**, 21851 (2017).
[39] R. Shiloh, R. Remez, P.-H. Lu, L. Jin, Y. Lereah, A. H. Tavabi, R. E. Dunin-Borkowski, and A. Arie, Spherical aberration correction in a scanning transmission electron microscope using a sculpted thin film, Ultramicroscopy **189**, 46 (2018).
[40] F. S. Yasin, T. R. Harvey, J. J. Chess, J. S. Pierce, and B. J. McMorran, Path-separated electron interferometry in a scanning transmission electron microscope, J. Phys. D: Appl. Phys. **51**, 205104 (2018).
[41] $(f(x)e^{ikx}) \otimes g(x) = [f(x) \otimes (g(x)e^{-ikx})]e^{ikx}$.
[42] Inelastic and very-high-angle scattering reduce the amplitude of the coherent electron wave function.
[43] H. Lichte and M. Lehmann, Electron holography–basics and applications, Rep. Prog. Phys. **71**, 016102 (2008).
[44] E. J. Kirkland, *Advanced Computing in Electron Microscopy* (Springer Science & Business Media, New York, NY, USA, 2010).
[45] Z. Tang, N. A. Kotov, and M. Giersig, Spontaneous organization of single CdTe nanoparticles into luminescent nanowires, Science **297**, 237 (2002).
[46] J. Lee, T. Javed, T. Skeini, A. O. Govorov, G. W. Bryant, and N. A. Kotov, Bioconjugated Ag nanoparticles and CdTe nanowires: metamaterials with field-enhanced light absorption, Angew. Chemie Int. Ed. **45**, 4819 (2006).
[47] C. Ricolleau, Y. Le Bouar, H. Amara, O. Landon-Cardinal, and D. Alloyeau, Random vs realistic amorphous carbon models for high resolution microscopy and electron diffraction, J. Appl. Phys. **114**, 213504 (2013).
[48] C. Ophus, A fast image simulation algorithm for scanning transmission electron microscopy, Adv. Struct. Chem. Imaging **3**, 13 (2017).
[49] A. Pryor, C. Ophus, and J. Miao, A streaming multi-GPU implementation of image simulation algorithms for scanning transmission electron microscopy, Adv. Struct. Chem. Imaging **3**, 15 (2017).
[50] F. Yasin, T. Harvey, J. J. Chess, J. S. Pierce, C. Ophus, P. Ercius, and B. McMorran, Probing light atoms at sub-nanometer resolution: realization of scanning transmission electron microscope holography, Nano Lett. **18**, 7118 (2018).
[51] O. Kfir, S. Zayko, C. Nolte, M. Sivis, M. Möller, B. Hebler, S. S. P. K. Arekapudi, D. Steil, S. Schäfer, M. Albrecht, O. Cohen, S. Mathias, and C. Ropers, Nanoscale magnetic imaging using circularly polarized high-harmonic radiation, Sci. Adv. **3**, eaao4641 (2017).